Noise mitigation for high-sensitivity phase estimation based on weak measurements

Xiaorui Tan,[1] Hongjing Li,[1,2,3,*] Qi Song,[1] Chunhui Shi,[1] Qingxin Deng,[1] Binke Xia,[1] Zhongyuan Luo,[1] Jingzheng Huang,[1,2,3] and Guihua Zeng[1,2,3]

[1]*State Key Laboratory of Advanced Optical Communication Systems and Networks, Institute for Quantum Sensing and Information Processing, School of Sensing Science and Engineering, Shanghai Jiao Tong University, Shanghai 200240, People's Republic of China*

[2]*Hefei National Laboratory, Hefei 230088, People's Republic of China*

[3]*Shanghai Research Center for Quantum Sciences, Shanghai 201315, People's Republic of China*

(Received 30 October 2023; accepted 12 April 2024; published 8 May 2024)

Phase estimation has attracted much attention in the field of sensing, where weak measurement has become an effective solution for the study of small physical quantities because of its anomalous amplification property. However, it is difficult for weak measurement to cope with large low-frequency noise signals in the environment due to its extremely narrow linear range, which makes the extension of weak measurement to practical applications a challenging task. In order to solve this issue, we propose and experimentally verify a phase demodulation scheme based on weak measurement, which solves the problem of working point offset caused by the noise through artificially introducing a high-frequency carrier and performing demodulation operations on the output light. The experimental results show that the scheme can improve the signal-to-noise ratio by 17 dB compared to standard weak measurement and ensures low distortion in phase demodulation. Moreover, the scheme is not limited to a specific modulation depth, which greatly improves the robustness of the scheme.

DOI: 10.1103/PhysRevA.109.053512

I. INTRODUCTION

Precise estimation of the optical phase is a difficult and important task, which plays an essential role in many fields, such as gravitational wave detection [1], angular momentum measurement [2], and biological imaging [3]. In order to achieve better phase estimation, researchers are committed to constantly improving the optical system by seeking effective noise suppression and signal enhancement methods [4,5]. One of the main obstacles to measurement is the inevitable noise inherent in the actual optical system, which drowns out or disturbs the measured phase, making the extraction of useful information difficult [6].

As a technique widely used for the precise measurement of weak physical parameters [7–11], weak measurement (WM) enables anomalous amplification of a small optical phase at the cost of postselection probability, which improves sensing sensitivity by three orders of magnitude over standard interferometry [12] while suppressing several kinds of technical noise to improve the signal-to-noise ratio (SNR) [13]. Meanwhile, WM with light intensity detection can be used to estimate real-time time-varying and unknown parameters [14].

The parameter to be measured reflects the interaction strength between the system and the pointer, and when the interaction strength satisfies the WM condition, the WM system works in the linear range, which ensures the high-sensitivity measurement [14,15]. However, a weak to strong interaction strength leads to a transition of the WM working region from linear to nonlinear, which affects the extraction of the parameter to be measured [16–18]. The phase of the output light contains not only the estimated phase, but also the initial phase and the phase caused by external environmental noise in practical applications. The noise phases will make the estimated phase move to a nonoptimal working point or nonlinear region, which seriously affects the sensitivity of the phase measurement [19,20]. The nonlinear errors caused by the mentioned problem can be effectively solved by the phase demodulation technology in classical fiber optic sensing so that the precision and stability of measurement are improved [21,22]. Thus weak measurement may have the potential to show its performance advantages in more scenarios with a phase demodulation technology suitable for it.

The selection and optimization of the phase demodulation technology largely determines the performance of the sensing, which typically determines important indicators such as sensitivity, resolution, and stability of the sensing [23,24]. As one of the widely applied demodulation technologies in the field of sensing, the phase-generated carrier (PGC), whose core idea is artificially generating a large-amplitude and deterministic sinusoidal phase signal outside the bandwidth of the estimated phase in the light phase, can stably recover the estimated phase in the presence of the interference phases regardless of the working point, which has the advantages of high sensitivity, a large dynamic range, and great linearity [22,25,26].

In this paper we propose a phase demodulation scheme based on WM to achieve noise mitigation for high-sensitivity estimation of the time-varying phase, which we call the WM PGC scheme. Specifically, our scheme achieves amplification of the small phase and suppresses technical noises, thus enhancing the sensitivity of measurement while suppressing

*lhjnet2012@sjtu.edu.cn

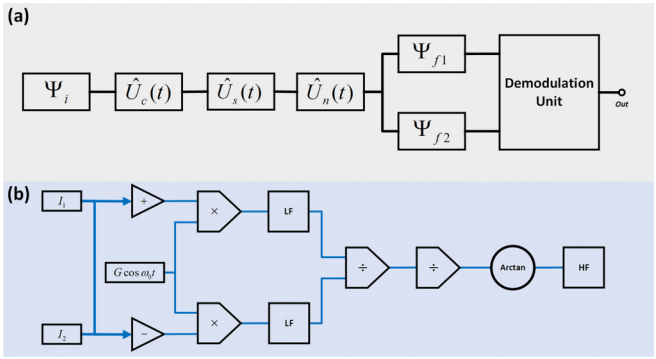

FIG. 1. (a) Schematic diagram of the WM PGC. (b) Principle of the WM PGC's demodulation unit. The following denotations are used: LF, low-pass filter; HF: high-pass filter; and Acrtan, arctangent operation.

demodulated phase fading and distortion caused by the initial phase and low-frequency environmental noise. Moreover, the demodulation unit of the WM PGC scheme does not have to be limited to a specific modulation depth C compared to typical PGC methods, greatly increasing the robustness of the scheme.

The rest of this paper is organized as follows. In Sec. II we present a theoretical model of the WM PGC scheme and illustrate the feasibility of the scheme via numerical simulations. In Sec. III we experimentally verify the noise mitigation and antidistortion capability of the WM PGC scheme. We briefly summarize in Sec. IV.

II. THEORY AND SIMULATION OF THE WM PGC SCHEME

In this section we demonstrate the theoretical model of the WM PGC scheme. In a standard WM system, the estimated signal is encoded into a phase parameter in the interaction process, which introduces $\varphi_s(t)$ between $|H\rangle$ and $|V\rangle$, where $|H\rangle$ and $|V\rangle$ represent the horizontal and vertical polarization states, respectively. By setting the suitable pre- and postselection states $|\Psi_i\rangle$ and $|\Psi_f\rangle$, $\varphi_s(t)$ can be amplified proportionally by the weak value $A_w = \frac{\langle\Psi_i|\hat{A}|\Psi_i\rangle}{\langle\Psi_f|\Psi_i\rangle}$, thus increasing the sensitivity of the measurement, where $\hat{A} = |H\rangle\langle H| - |V\rangle\langle V|$ is one of Pauli matrices acting on the system.

However, the amplification of $\varphi_s(t)$ requires that it is within the extremely narrow linear range of the measurement. Initial phase drift and external low-frequency noise in actual measurements can cause $\varphi_s(t)$ to deviate from the linear range, which makes phase estimation inaccurate and unstable and thus lose the performance advantages of WM. Therefore, it is highly necessary to suppress the above issues for precise and sensitive demodulation of the estimated phases.

The schematic diagram of the WM PGC scheme is shown in Fig. 1(a). The light beam is preselected to a 45° linear polarization state

$$|\Psi_i\rangle = \frac{\sqrt{2}}{2}(|H\rangle + |V\rangle). \tag{1}$$

In the interaction process, besides the estimated signal $\varphi_s(t)$, a carrier signal $\varphi_c(t) = C\cos\omega_0 t$ is artificially introduced and the noise signal $\varphi_n(t)$ is considered, where C is the modulation depth, ω_0 is the carrier frequency, and $\varphi_n(t)$ includes the initial phase and the external noise. The process of the three signals being encoded into the phase can be represented by unitary operators

$$\begin{aligned}\hat{U}_c(t) &= e^{-i\varphi_c(t)\hat{A}},\\ \hat{U}_s(t) &= e^{-i\varphi_s(t)\hat{A}},\\ \hat{U}_n(t) &= e^{-i\varphi_n(t)\hat{A}},\end{aligned} \tag{2}$$

and the light beam evolves into

$$|\Psi(t)\rangle = \hat{U}_n(t)\hat{U}_s(t)\hat{U}_c(t)\,|\Psi_i\rangle\,. \tag{3}$$

In the postselection process, the light beam enters two different postselection paths, both of which are set to be almost orthogonal to the preselection state

$$|\Psi_{f1,2}\rangle = \frac{\sqrt{2}}{2}(e^{i\varepsilon_{1,2}}\,|H\rangle - e^{-i\varepsilon_{1,2}}\,|V\rangle), \tag{4}$$

where $\varepsilon_{1,2} = \pm\varepsilon$ is the postselection angle of each path, $|\varepsilon| \ll 1$.

The evolved state is projected to the two different final states after the postselection process. Then the light intensity of each path is

$$I_{1,2}(t) = \frac{I_0}{2}|\langle\Psi_{f1,2}|\Psi(t)\rangle|^2, \tag{5}$$

where I_0 is the initial light intensity. The specific expressions are

$$\begin{aligned}I_1(t) =& \tfrac{1}{4}I_0\{1 - \cos 2\varepsilon\cos[C\cos\omega_0 t + \varphi(t)]\\ &+ \sin 2\varepsilon\sin(C\cos\omega_0 t + \varphi(t))]\},\\ I_2(t) =& \tfrac{1}{4}I_0\{1 - \cos 2\varepsilon\cos[C\cos\omega_0 t + \varphi(t)]\\ &- \sin 2\varepsilon\sin(C\cos\omega_0 t + \varphi(t))]\},\end{aligned} \tag{6}$$

where $\varphi(t) = \varphi_s(t) + \varphi_n(t)$.

Then the two output lights enter the demodulation unit for data processing to demodulate the time-varying estimated phase $\varphi_s(t)$, whose principle of demodulation is shown in Fig. 1(b). The $I_1(t)$ and $I_2(t)$ perform the summation and difference operation:

$$\begin{aligned}I_a(t) &= \frac{I_0}{2}\{1 - \cos 2\varepsilon\cos[C\cos\omega_0 t + \varphi(t)]\},\\ I_b(t) &= \frac{I_0}{2}\sin 2\varepsilon\sin[C\cos\omega_0 t + \varphi(t)].\end{aligned} \tag{7}$$

By multiplying both $I_a(t)$ and $I_b(t)$ by $G\cos\omega_0 t$ for mixing and passing them through low-pass filters, a pair of nonstrictly quadrature components can be obtained. Here $\alpha(t)$ corresponds to $I_a(t)$, while $\beta(t)$ corresponds to $I_b(t)$,

$$\begin{aligned}\alpha(t) &= \frac{I_0}{2}\cos 2\varepsilon\, GJ_1(C)\sin\varphi(t),\\ \beta(t) &= \frac{I_0}{2}\sin 2\varepsilon\, GJ_1(C)\cos\varphi(t),\end{aligned} \tag{8}$$

where $J_1(C)$ is the first-order Bessel function with C. We define a parameter $\Re$ from which the phase $\varphi(t)$ can be demodulated which can be derived by dividing $\alpha(t)$ and $\beta(t)$:

$$\Re(t) = \frac{\alpha(t)}{\beta(t)} = \cot 2\varepsilon \tan \varphi(t). \tag{9}$$

Then we divide $\Re(t)$ by the amplification factor $\cot 2\varepsilon$ and perform the arctangent operation to obtain $\varphi(t)$:

$$\varphi(t) = \arctan \frac{\Re(t)}{\cot 2\varepsilon}. \tag{10}$$

Finally, the estimated phase $\varphi_s(t)$ is obtained after passing through a high-pass filter.

From the above derivation process, it can be concluded that the postselection attenuates the average light intensity, reduces the noise introduced by technical problems (e.g., light power fluctuation and device defects), and amplifies the small phase (9), which significantly enhances the SNR and enables more accurate estimation of the small phase [27].

When $\varphi(t) \ll 1$, the sensitivity of the WM PGC scheme is $\frac{\partial \Re(t)}{\partial \varphi(t)} \approx \cot 2\varepsilon$. The smaller the postselection angle ε is preset, the higher the measurement sensitivity could be. The setting of ε is limited by the experimental conditions, such as the resolution of the detector and the extinction ratio of the polarizer; hence a trade-off has to be made in the experiment.

In addition, the measurement sensitivity and the linear range are bound to each other in standard WM. The smaller the postselection angle, the higher the sensitivity but the narrower the linear range. For comparison, the reduction of the postselection angle in the WM PGC scheme improves the measurement sensitivity while the linear range remains unchanged. The WM PGC scheme has a wider linear range than standard WM when the linearity is the same while ensuring phase amplification on the same order of magnitude, which means it can handle stronger signal amplitude and meet the requirements better in practical applications, as shown in Fig. 2.

We use simulation and numerical analysis to illustrate the excellent demodulation performance of the WM PGC scheme. The basic simulation parameters are set as follows. The sampling rate is 400 kHz. The initial light intensity is $I_0 = 50$ mW. The angle of the postselection is $\varepsilon = 0.01$ rad. The carrier φ_c is set to $1.84\cos(2\pi \times 50\,000t)$. The estimated phase φ_s is set to $10^{-3}\cos(2\pi \times 2000t)$. The noise phase φ_n is set to $10^{-3}\cos(2\pi \times 100t) + 5 \times 10^{-2}\cos(2\pi \times 50t) + 10^{-2}\cos(2\pi \times 10t) + 10^{-1}\cos(2\pi \times 5t)$. The amplitude of the fundamental frequency signal for mixing is set to $G = 1$. The simulation results are shown in Fig. 3.

Figure 3(a) represents the noise-containing phase signal $\varphi(t)$, i.e., $\varphi(t) = \varphi_s(t) + \varphi_n(t)$, obtained by the two schemes, respectively. It can be seen that standard WM is limited by its narrow dynamic range and cannot cope with signals with large amplitude, while the WM PGC scheme can demodulate $\varphi_s(t)$ and $\varphi_n(t)$ without distortion. Then the $\varphi(t)$ demodulated by both schemes are passed through a high-pass filter in order to obtain $\varphi_s(t)$, as shown in Fig. 3(b) (only 20 periods are shown in the figure). The $\varphi_s(t)$ demodulated by the WM PGC scheme after filtering basically matches the theoretical curve.

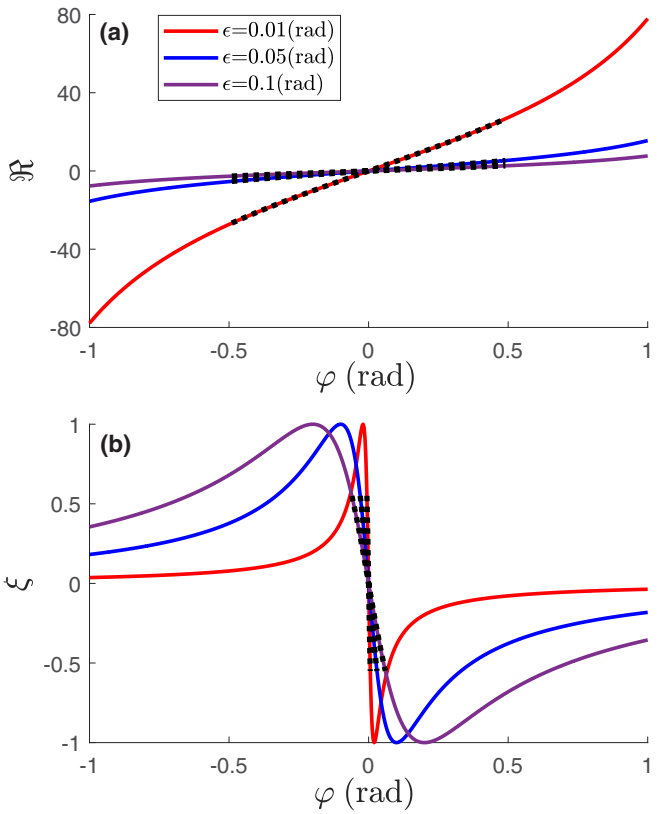

FIG. 2. (a) Relationship between the observable $\Re$ and phase φ in the WM PGC scheme. (b) Relationship between the observable ξ and phase φ in standard WM [14]. The red, blue, and purple solid lines indicate the relationship curves when the postselection angle is $\epsilon = 0.01$, 0.05, and 0.1 rad, respectively. The black dotted lines indicate the linear range of each curve.

On the contrary, large low-frequency noise signals $\varphi_n(t)$ cause the $\varphi_s(t)$ demodulated by the standard WM to be flipped and the amplitude to be inaccurate and fluctuating. In order to better demonstrate the demodulation performance of the WM PGC scheme numerically, the mean absolute error (MAE) and root-mean-square error (RMSE) are introduced as metrics for evaluating the error between the estimated values and the true values, as shown in Table I. The calculation results show that our scheme is more robust in the presence of large low-frequency noise and has the potential to cope with a wider range of application scenarios.

III. EXPERIMENT AND RESULTS

Our experimental setup is shown in Fig. 4. We use a narrow linewidth and ultralow-noise laser (Thorlabs ULN15TK, 100 Hz@linewidth) as the light source, yielding continuous light

TABLE I. Errors for the phase estimation with the WM PGC and standard WM.

Scheme	MAE (μrad)	RMSE (μrad)
WM PGC	0.2347	1.3185
standard WM	30.4071	154.2435

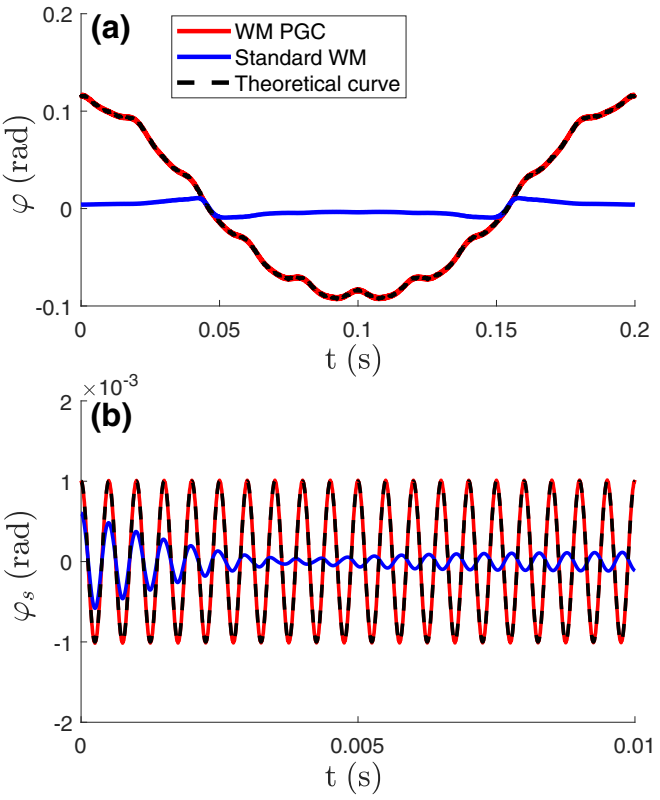

FIG. 3. (a) Noise-containing phase signal $\varphi(t)$ demodulated by the WM PGC scheme and standard WM. (b) Estimated phase signal $\varphi_s(t)$ demodulated by the WM PGC scheme and standard WM. The red solid lines indicate the demodulation results of the WM PGC scheme, while the blue solid lines indicate the demodulation results of the standard WM. The black dashed line in (a) denotes the theoretical curve of $\varphi(t)$, while the black dashed line in (b) denotes the theoretical curve of $\varphi_s(t)$.

at a wavelength of 1550 nm. After passing through the isolator that prevents the backward transmitted light from affecting the source, the light beam is preselected to the 45° linear polarization at the fiber optic polarizer.

The key to the PGC method is the introduction of a high-frequency carrier in the light phase. Conventional PGC methods typically use either a piezoelectric transducer to modulate one arm of the interferometer (external

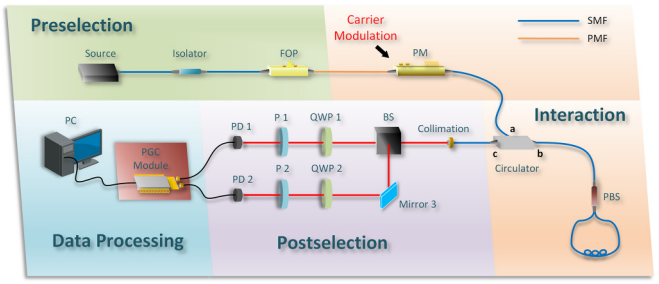

FIG. 4. Optical setup diagram: FOP, fiber optic polarizer; PM, phase modulator; PBS, polarization beam splitter; BS, beam splitter; QWP, quarter waveplate; P, polarizer; PD, photodetector; SMF, single-mode fiber; and PMF, polarization-maintaining fiber.

TABLE II. SNR and THD of the demodulation signals.

Scheme	SNR (dB)	THD (dB)
WM PGC	24.5119	−42.4312
standard WM	7.4815	−16.2362

modulation) [28] or current to modulate the laser frequency (internal modulation) [29] to generate the carrier. The former approach introduces electrical devices in the sensing unit, which is not conducive to applications in complicated environments and yields additional electrical noise, while the latter causes a decrease in demodulation reliability due to the accompanying amplitude modulation phenomenon. Here we use a $LiNbO_3$ phase modulator (Thorlabs LN53S-FC) to yield the carrier $\varphi_c(t) = C\cos\omega_0 t$ at an amplitude of $C = 1.84$ rad and a frequency of $\omega_0 = 50$ kHz directly in the light phase, which makes operation easy and avoids unnecessary amplitude modulation [20]. It is worth noting that the phase modulator introduces the carrier phase between the ordinary and extraordinary modes, which can be extracted after postselection.

The light beam enters through port a of the circulator after the introduction of the carrier and is first sent out through port b to a Sagnac interferometer structure for sensing. When the light beam passes through the polarization beam splitter (PBS), it is divided into $|H\rangle$ and $|V\rangle$; here $|H\rangle$ and $|V\rangle$ denote parallel and perpendicular to the fiber axis, respectively. External signals act on the sensing unit, leading to the phase difference between $|H\rangle$ and $|V\rangle$ when they are recombined at the PBS. We use a single-frequency sinusoidal signal with a frequency of 7 kHz as the time-varying estimated phase $\varphi_s(t)$, and the initial phase and the low-frequency interference from the external environment are combined into the noise phase $\varphi_n(t)$, where the external interference is the artificially generated low-frequency vibration.

The combined light beam comes out of port c and enters the postselection process. The beam is split by the beam splitter into two postselection paths, each of which has a quarter waveplate and a polarizer playing an important role. The fast axes of both quarter waveplates QWP1 and QWP2 are set to 45°. The optical axis of polarizer P1 is set to differ by $\varepsilon_1 = \varepsilon$ deg from −45°, while the optical axis of polarizer P2 is set to differ by $\varepsilon_2 = -\varepsilon$ deg from −45°, where $\varepsilon = 0.01$ rad, at which point both postselections are approximately orthogonal to the preselection. After the postselection, the two output lights enter the PGC module for data processing and are finally demodulated to obtain the $\varphi_s(t)$. Here the sampling frequency is set to 200 kHz and the measurement time is 10 s. The WM PGC scheme can perform higher measurement precision and sensitivity in the presence of interference than standard WM, as shown in Fig. 5.

To demonstrate more clearly the great measurement performance of the WM PGC scheme, we introduce the SNR and total harmonic distortion (THD) as metrics to compare them, as shown in Table II. Total harmonic distortion is defined as the ratio of the equivalent root-mean-square amplitude of all harmonics to the fundamental amplitude of the estimated signal $\frac{\sqrt{\sum_{i=2}^{\infty} P_i^2}}{P_1}$, where P_1 and P_i are the amplitudes of the

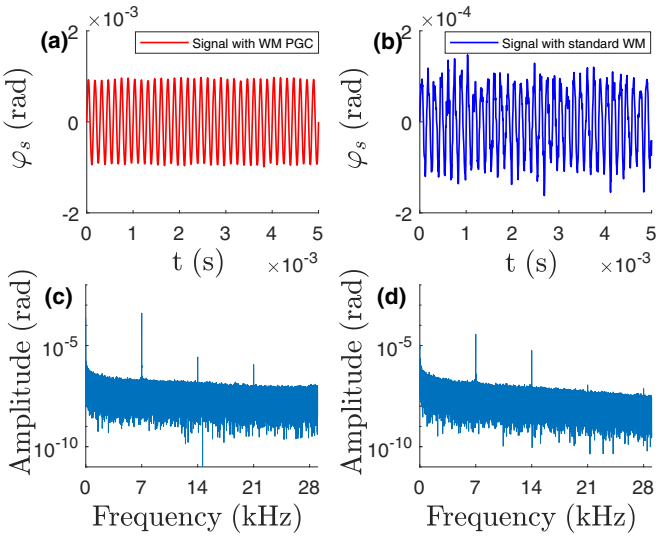

FIG. 5. (a) Time-domain diagram of $\varphi_s(t)$ demodulated by the WM PGC scheme. (b) Time-domain diagram of $\varphi_s(t)$ demodulated by the standard WM. (c) Spectrum of $\varphi(t)$ demodulated by the WM PGC scheme. (d) Spectrum of $\varphi(t)$ demodulated by the standard WM. Both time-domain diagrams of $\varphi_s(t)$ show a time length of only 5 ms.

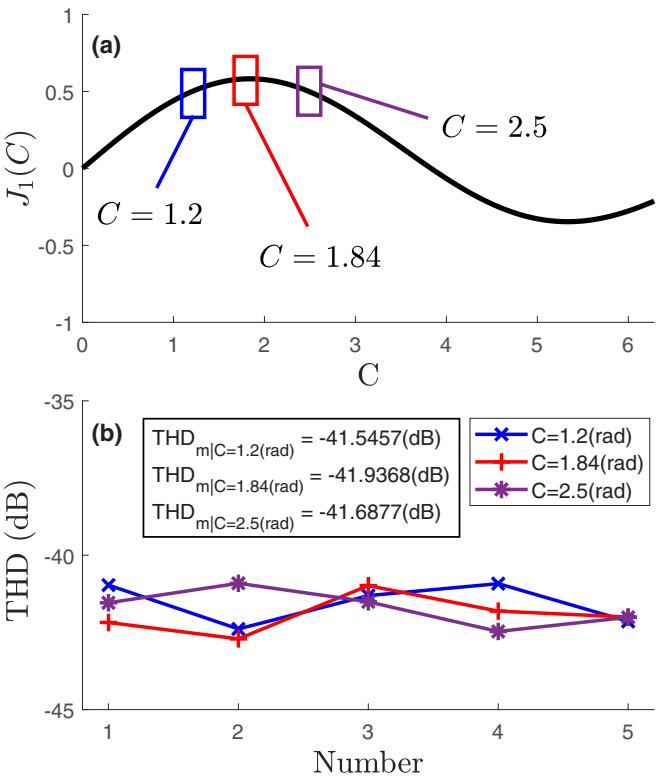

FIG. 6. (a) Curve of the first-order Bessel function. (b) THD of demodulated signals at different modulation depths C. The mean THD of demodulated signals at $C = 2.5$, 1.84, and 1.2 rad is −41.6877, −41.9368, and −41.5457 dB, respectively.

fundamental frequency and the ith harmonic, respectively. The WM PGC scheme improves the SNR by about 17 dB, with a THD of only −42.4 dB, which means it ensures higher measurement sensitivity and has a strong capability of distortion resistance. Moreover, we perform ten measurements using the WM PGC scheme and the results show a SNR of 24.9 ± 1.1 dB and a THD of -42.6 ± 1.7 dB for these ten measurements.

The selection of modulation depth C is an important issue in the PGC technology, which determines the stability of the demodulation. In the conventional PGC DCM (differential and cross multiplying) method and the PGC arctan method, the modulation depth must be adjusted to $C = 2.37$ and 2.63 rad, respectively; otherwise the demodulation result will have severe nonlinear errors [30,31]. In contrast, because only the fundamental carrier is used for mixing in the WM PGC scheme, only $J_1(C)$ remains in the coefficients after low-pass filtering, and it is removed in the first divider (9), which greatly reduces the impact of C on demodulation performance. By observing the curve of $J_1(C)$, it is known that $C = 1.84$ is the first extreme point of $J_1(C)$, as shown in Fig. 6(a), where the slight fluctuation of C has little effect on the value of $J_1(C)$, which is the reason why the C value is preset to 1.84 rad in the experiment above. In order to thoroughly analyze the demodulation performance of the WM PGC scheme with different modulation depths, three different C values are set in our experiments, $C = 2.5$, 1.84, and 1.2 rad, respectively. We use THD as the metric to evaluate the distortion levels of the demodulated phase at different C values, and each C value is measured five times, each time for 10 s, as shown in Fig. 6(b). The experimental results show that choosing different modulation depths C has little effect on the distortion degree of the demodulated phase, which means that the WM PGC scheme can be used without sticking to a specific C and is robust to the drift of C.

IV. CONCLUSION

In order to achieve more precise and sensitive measurement of the time-varying optical phase, we proposed a phase demodulation scheme based on WM and conducted experiments to verify it. Theoretical derivation and simulation verification showed that the WM PGC scheme possesses a wider linear range than standard WM and also guarantees a phase amplification magnitude consistent with it. The experimental results demonstrated that the WM PGC scheme improves the SNR by 17 dB and has a strong capability of distortion resistance, significantly enhancing the sensitivity of measurement. Moreover, it was experimentally demonstrated that the WM PGC scheme is not bound to a specific value of the modulation depth C, which greatly improves the robustness of the scheme. The WM PGC scheme provides a different perspective of the expansion of WM into practical applications.

ACKNOWLEDGMENTS

This work was supported by the National Natural Science Foundation of China (Grant No. 62071298), Innovation Program for Quantum Science and Technology (Grant No. 2021ZD0300703), and Shanghai Municipal Science and Technology Major Project (Grant No. 2019SHZDZX01).

[1] H. Grote, R. Schnabel, and H. Vahlbruch, A gravitational wave observatory operating beyond the quantum shot-noise limit, Nat. Phys. **7**, 962 (2011).

[2] G. Puentes, N. Hermosa, and J. P. Torres, Weak measurements with orbital-angular-momentum pointer states, Phys. Rev. Lett. **109**, 040401 (2012).

[3] D. Huang, E. A. Swanson, C. P. Lin, J. S. Schuman, W. G. Stinson, W. Chang, M. R. Hee, T. Flotte, K. Gregory, C. A. Puliafito *et al.*, Optical coherence tomography, Science **254**, 1178 (1991).

[4] B. Crockett, L. R. Cortés, R. Maram, and J. Azaña, Optical signal denoising through temporal passive amplification, Optica **9**, 130 (2022).

[5] G. Zheng, X. Cui, and C. Yang, Surface-wave-enabled dark-field aperture for background suppression during weak signal detection, Proc. Natl. Acad. Sci. USA **107**, 9043 (2010).

[6] R. A. Yotter and D. M. Wilson, A review of photodetectors for sensing light-emitting reporters in biological systems, IEEE Sens. J. **3**, 288 (2003).

[7] O. Hosten and P. Kwiat, Observation of the spin Hall effect of light via weak measurements, Science **319**, 787 (2008).

[8] B. Xia, J. Huang, C. Fang, H. Li, and G. Zeng, High-precision multiparameter weak measurement with Hermite-Gaussian pointer, Phys. Rev. Appl. **13**, 034023 (2020).

[9] L. Z. Liu, Y. Z. Zhang, Z. D. Li, R. Zhang, X. F. Yin, Y. Y. Fei, L. Li, N. L. Liu, F. Xu, Y. A. Chen *et al.*, Distributed quantum phase estimation with entangled photons, Nat. Photon. **15**, 137 (2021).

[10] H. Li, J. Z. Huang, Y. Yu, Y. Li, C. Fang, and G. Zeng, High-precision temperature measurement based on weak measurement using nematic liquid crystals, Appl. Phys. Lett. **112**, 231901 (2018).

[11] Q. Song, B. Xia, J. Huang, T. Xiao, H. Li, and G. Zeng, Surpassing the Nyquist sampling limit via postmodulation, Phys. Rev. Appl. **18**, 034077 (2022).

[12] N. Brunner and C. Simon, Measuring small longitudinal phase shifts: Weak measurements or standard interferometry? Phys. Rev. Lett. **105**, 010405 (2010).

[13] A. N. Jordan, J. Martínez-Rincón, and J. C. Howell, Technical advantages for weak-value amplification: When less is more, Phys. Rev. X **4**, 011031 (2014).

[14] Q. Song, H. Li, J. Huang, T. Xiao, X. Tan, B. Xia, and G. Zeng, Adaptive time-varying parameter estimation via weak measurement, Phys. Rev. Appl. **18**, 044031 (2022).

[15] Z. H. Zhang, G. Chen, X. Y. Xu, J. S. Tang, W. H. Zhang, Y. J. Han, C. F. Li, and G. C. Guo, Ultrasensitive biased weak measurement for longitudinal phase estimation, Phys. Rev. A **94**, 053843 (2016).

[16] M. Szyniszewski, A. Romito, and H. Schomerus, Entanglement transition from variable-strength weak measurements, Phys. Rev. B **100**, 064204 (2019).

[17] F. Piacentini, A. Avella, M. Gramegna, R. Lussana, F. Villa, A. Tosi, G. Brida, I. P. Degiovanni, and M. Genovese, Investigating the effects of the interaction intensity in a weak measurement, Sci. Rep. **8**, 6959 (2018).

[18] Y. Pan, J. Zhang, E. Cohen, C.-w. Wu, P.-X. Chen, and N. Davidson, Weak-to-strong transition of quantum measurement in a trapped-ion system, Nat. Phys. **16**, 1206 (2020).

[19] G. Wang, H. Li, T. Xiao, J. Huang, and G. Zeng, Adaptive correction of phase estimation with time based on weak measurement, Opt. Express **29**, 39150 (2021).

[20] F. Karim, Y. Zhu, and M. Han, Modified phase-generated carrier demodulation of fiber-optic interferometric ultrasound sensors, Opt. Express **29**, 25011 (2021).

[21] A. Dandridge, A. B. Tveten, and T. G. Giallorenzi, Homodyne demodulation scheme for fiber optic sensors using phase generated carrier, IEEE Trans. Microw. Theory **30**, 1635 (1982).

[22] Y. Marin, P. Velha, and C. J. Oton, Distortion-corrected phase demodulation using phase-generated carrier with multitone mixing, Opt. Express **28**, 36849 (2020).

[23] Y. Dong, P.-C. Hu, H. Fu, H. Yang, R. Yang, and J. Tan, Long range dynamic displacement: Precision PGC with sub-nanometer resolution in an LWSM interferometer, Photon. Res. **10**, 59 (2022).

[24] E. Udd and W. B. Spillman, Jr., *Fiber Optic Sensors: An Introduction for Engineers and Scientists* (Wiley, New York, 2011).

[25] A. V. Volkov, M. Y. Plotnikov, M. V. Mekhrengin, G. P. Miroshnichenko, and A. S. Aleynik, Phase modulation depth evaluation and correction technique for the PGC demodulation scheme in fiber-optic interferometric sensors, IEEE Sens. J. **17**, 4143 (2017).

[26] J. He, L. Wang, F. Li, and Y. Liu, An ameliorated phase generated carrier demodulation algorithm with low harmonic distortion and high stability, J. Lightw. Technol. **28**, 3258 (2010).

[27] X. Qiu, L. Xie, X. Liu, L. Luo, Z. Li, Z. Zhang, and J. Du, Precision phase estimation based on weak-value amplification, Appl. Phys. Lett. **110**, 071105 (2017).

[28] Q. Lin, L. Chen, S. Li, and X. Wu, A high-resolution fiber optic accelerometer based on intracavity phase-generated carrier (PGC) modulation, Meas. Sci. Technol. **22**, 015303 (2011).

[29] X. Mao, X. Tian, X. Zhou, and Q. Yu, Characteristics of a fiber-optical Fabry–Perot interferometric acoustic sensor based on an improved phase-generated carrier-demodulation mechanism, Opt. Eng. **54**, 046107 (2015).

[30] Y. Muanenda, S. Faralli, C. J. Oton, C. Cheng, M. Yang, and F. Di Pasquale, Dynamic phase extraction in high-SNR DAS based on UWFBGs without phase unwrapping using scalable homodyne demodulation in direct detection, Opt. Express **27**, 10644 (2019).

[31] L. Wang, M. Zhang, X. Mao, and Y. Liao, in *Interferometry XIII: Techniques and Analysis*, edited by E. L. Novak, W. Osten, and C. Gorecki, SPIE Proc. Vol. 6292 (SPIE, Bellingham, 2006), pp. 439–448.